Journal of Solar Energy Research (JSER)

JSER

Grid-Connected Fuel Cell Power Quality Improvement System Control Based on Phase Compensator on Capacitor Current Feedback Active Damping

Majid Hosseinpour[a], Shahab Sajedi[b]

[a]*Department of Electrical and Computer Engineering, University of Mohaghegh Ardabili, Ardabil, Iran*
[b]*School of Electrical and Electronic Engineering, University College Dublin, Dublin, Ireland*

ARTICLE INFO

ABSTRACT

Recently, fuel cells (FC) have received attention due to their environmental benefits and applications in distributed generation systems. Voltage source inverters interconnect the FCs to the power grid. In this paper, the capacitor current feedback (CCF) method is utilized to dampen the LCL filter's inherent resonance, and a phase compensator in the CCF path is used to compensate for the undesirable effects of the control delay of the grid-connected FC power quality improvement system. With this trick, a virtual RC network is paralleled by the filter capacitor, effectively increasing the range of the VPRR without changing the instances of sampling. To check the performance correctness of the suggested method, the design of each section is introduced for the phase compensation and the parameters of the closed-loop system under study. With this trick, the prohibited range of the LCL filter's resonance frequency is deleted, and the limitation of the resonance frequency is removed. The results of the low-voltage grid-connected FC power quality improvement system with the suggested control method reveal that the stability of system is maintained with changes in the network impedance. Also, the injected current's quality is very suitable even in the harmonically weak network.

1. Introduction

Conventional power generation systems are undergoing a significant transformation, and distributed energy resources (DERs) account for a more significant share than fossil fuel-based energy resources [1]. Distributed generation resources such as solar, wind, or fuel cells can operate in grid-

*Corresponding Author Email:hoseinpour.majid@uma.ac.ir

connected or stand-alone mode [2]. Between the various types of distributed generation resources, Fuel cells (FC) can be installed anywhere without environmental barriers. Fuel cells are electrochemical energy transformation instruments that produce electrical energy from chemical energy. In recent years, research in the fuel cell field has increased, and FCs have been utilized in various applications such as electric vehicles, airplanes, power injection into the grid, and other miscellaneous industries [3]. Solid Oxide FCs (SOFC), Molten Carbonate FCs (MCFC), Alkaline FCs (AFC), Phosphoric Acid FCs (PAFC), and Proton Exchange Membrane FCs (PEMFC) are the most common and widespread types of FCs. Among the various available FC technologies, high-temperature FCs, such as SOFC and MCFC, are primarily used to produce large-scale FC power plants. SOFC and MCFC have higher efficiency and can quickly respond to the required load changes, and the proton exchange membrane FC is suitable for connecting to the power grid in the scale of tens of kilowatts [4-5].

Fuel cells are widely used in grid-connected mode, and several control schemes have been utilized for fuel cell-based power conditioning systems. Han et al. [6] have proposed an iteration-based controller for a current source converter with dual half-bridge modules (CF-DHB) for a grid-tied FC system. Since the transfer function of the duty cycle to the DC link voltage has a right half-plane zero (RHP), the conventional PI controller cannot control the DC link voltage optimally. Hence, a repetitive controller has been employed to control the DC link voltage and to eliminate the phase delay caused by the presence of the right half-plane zero, a phase-lead compensator has been used. Sabir [7] has presented a robust control scheme for the power electronic converter to interconnect the FC power generation system to the grid. The control strategy of this paper is employed without the need for a phase-locked-loop (PLL) under unbalanced network conditions. Baltacı et al. [8] have investigated the transferring of FC-produced energy to the power network through a DC-DC chopper and inverter using the conventional PI controller to inject high-quality current into the power network. The grid-tied FC using an LCL filter has been investigated by Rasekh et al. [9], and the control used in this study is based on the grid-side current feedback.

The voltage source inverter (VSI) is an essential interface among the power production unit and the power network in grid-tied applications [10-11]. High-order harmonic reduction of the grid current is essential for the grid-tied inverter, utilizing an L, LC, or LCL filter. The LCL filter has more acceptable harmonic weakening function than the LC and L filters [12], however, it has an intrinsic resonance characteristic that may cause system instability. To resolve this challenge, the inherent resonance of the LCL filter should be damped [13-14]. The resonance damping procedures caused by LCL filters are divided into two classes including active damping and passive damping procedures. The passive damping method employs a damping resistor in shunt or series with the filter inductor or capacitor, which leads to unacceptable power losses, especially in high-power applications. Since the active damping method only involves changes in the control loops and does not have additional power losses, it is more studied [15]. One of the active damping methods is based on state variable feedback [16], including several various schemes such as capacitor voltage feedback active damping [17], thorough state feedback active damping [18], and capacitor current feedback (CCF) active damping (AD) [19]. A cascade control structure, including a grid current outer control loop based on a conventional regulator and CCF inner control loop, is a common AD method [20-21]. Although the implementation of this active damping procedure is so simple, because of the presence of a high-precision capacitor current sensor, its hardware cost increases [22], and system reliability decreases [23].

Many grid-tied inverters are controlled digitally due to their remarkable flexibility. Due to digital control delay [24], the CCF damping performance is attenuated [25]. The CCF AD is equivalent to a frequency-dependent virtual resistance. In the frequency range where this virtual resistance acts as a negative resistance, the right poles appear in the system's transfer function and make the system unstable [26]. There are many ways to reduce the negative effects of digital control delays. A systematic design method is presented by Hosseinpour et al. [27] for robust control of an LCL-type grid-connected PEMFC system in a weak and harmonic grid. He et al. [28] is presented the control method based on capacitor-current proportional-integral positive feedback AD to extend the virtual positive resistance region (VPRR) up to the Nyquist frequency. However, using positive virtual feedback increases the risk of system instability. Chen et al. [29] is presented a compensation scheme based on area equivalence for active damping of LCL-type inverter. The compensator works without a complex design of parameters, but its efficiency is highly

dependent on the accuracy and performance of the DSP.

In this paper, to enhance the stability and current quality of the LCL-type grid-tied FC power quality improvement system, a phase compensator is utilized in the feedback of the capacitor current AD path. With this trick, a virtual RC network is paralleled by the filter capacitor, effectively increasing the range of the VPRR without changing the instances of sampling. With this trick, the prohibited range of the LCL filter resonance frequency is deleted, and the limitation of the resonance frequency is removed. With the accurate design for the parameters the closed loop system, the LCL-type grid-tied FC power quality improvement system can maintain its stability against network impedance changes and operate with considerable robustness, reliability, and safety against noise. The innovations of the paper include the following:

1. Provide a phase compensator with a simple structure and easy implementation for an LCL-type grid-connected FC power quality improvement system.
2. Explain how to remove the forbidden range of the resonance frequency of the LCL filter by the proposed phase compensator for performance system robustness in wide variations of grid impedance.
3. Provide a procedure for designing closed-loop control parameters of the system under study in the presence of the phase compensator.

The remain of this paper is set as outlined below. In the second section, the PEM fuel cell has been investigated. Then, the digital control delay negative influence is briefly reviewed. The third section proposes a phase compensator from the impedance point of view. It reveals the stability improvement advantages and the grid-tied inverter robustness. A complete design and determination method for the phase compensation and parameters of the closed loop system is presented in section four to ensure the grid-tied inverter stable operation against wide changes of grid impedance. The outcomes of the simulations are illustrated in section five to confirm the performance of the suggested phase compensator for the grid-connected fuel cell power quality improvement inverter and the proposed closed-loop parameter design method. Finally, a conclusion of the paper is presented in the sixth section.

2. General description of grid-connected system and effect of digital control delay

In this study, the proton exchange membrane fuel cell is considered a fuel cell power generation unit.

This type of fuel cell is the most well-known fuel cell exploited in applications connected to the low-voltage grid. This fuel cell is known as a power generation source with low amplitude voltage and high-capacity current characteristics. The electrical equivalent circuit of PEMFC is shown in Fig.1, and its behaviour is expressed by equations (1) to (4).
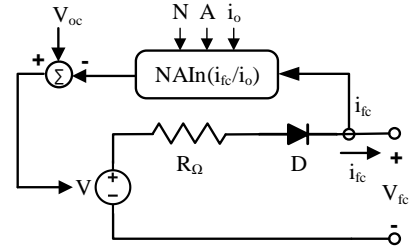

Figure 1. Electrical model of PEMFC fuel cell

The equivalent output voltage of the fuel cell is defined by equation (1) [30].

$$V_{fc} = V_{oc} - V_{\Omega} - V_d \tag{1}$$

where V_{fc} is the output voltage of the fuel cell stack, V_{oc} is the open circuit voltage, V_{Ω} is the resistive voltage drop, and V_d is the absolute polarization voltage drop. The open circuit voltage of the fuel cell is considered according to equation (2) [30].

$$V_{oc} = K_c \left[V_o + (T - 298) \frac{-44.43}{zF} + \frac{R_cT}{zF} \ln \left(\frac{P_{H_2} P_{O_2}^{1/2}}{P_{H_2O}} \right) \right] \tag{2}$$

The resistive voltage of the PEMFC is expressed according to equation (3), and the absolute polarization voltage is expressed according to equation (4) [30].

$$V_{\Omega} = i_{fc} R_{\Omega} \tag{3}$$

$$V_d = N \times A \times \ln(i_{fc}/i_o) \tag{4}$$

where N represents the number of cells. Besides, A is the *Tafel* slope, and i_o is the exchange current, as given in [30].

Fig. 2 illustrates the general scheme of the LCL-type grid-tied PEMFC power quality improvement system and its control system based on the CCF active damping. In this figure, v_g represents the network alternative voltage, $Z_g(s)$ is the network impedance and the amplitude as well as phase of the grid-injected reference current have been demonstrated respectively by I^* and θ, LCL filter parameters demonstrated by L_1, L_2, and C, H_{i1} and H_{i2} are the CCF and grid current coefficients respectively, in which both of them are positive values. The current regulator is demonstrated by $G_i(s)$.
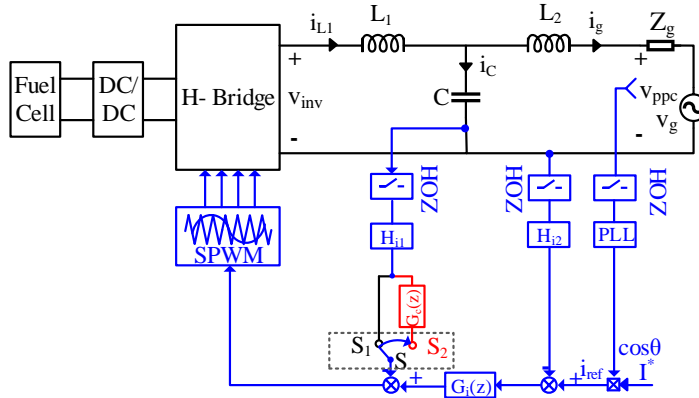
Figure 2. Schematic of the single-phase LCL-type grid-connected fuel cell power conditioning system with CCF

Considering the worst case to evaluate the passivity and stability of the grid-connected inverter, $Z_g(s)$ is considered an ideal inductor, which is included as sL_g. By connecting the switch S to the S_1 point, basic CCF active damping is achieved, where the current of the capacitor is sensed and considered in the current regulator output. By connecting the S switch to the S_2 point, the proposed method is activated. In this scheme, a phase compensator is assumed in the CCF path, and the result is added to the current regulator output.

The LCL-type grid-tied inverter control diagram using CCF active damping is demonstrated in [31]. As mentioned in [32], the digital control delay includes computational delay and delay of pulse width modulation. The computational delay, as z^{-1}, is the time interval between the instantaneous sampling of the signal and the immediate update of the modeled modulation waveform. Pulse width modulation delay is considered as $G_h(s) = (1 - e^{-sT_{sam}})/s \approx T_{sam}e^{-0.5sT_{sam}}$ which $T_s = 1/f_{sam}$ and $f_s = f_{sam}$ are the sampling period and sampling frequency, respectively.

According to Fig. 3, the CCF AD is equivalent to a virtual impedance Z_{ad-R-D} (not a pure resistance) in parallel with the filter capacitor, which $Z_{ad-R-D}(s)$ in [26] is written as follows:

$$Z_{ad-R-D}(s) = \frac{1}{Y_{ad-R-D}(s)} = \frac{1}{H_{i1}K_{PWM}} \cdot \frac{L_1}{C} \cdot \frac{T_{sam}}{G_h(s)} \cdot e^{sT_{sam}}$$

$$\square \ R_{ad} \ e^{1.5sT_{sam}}$$

(5)

where $Y_{ad-R-D}(s)$ is the related admittance, and R_{ad} is the related virtual and unreal resistance without considering the delay of digital control. Considering $s = j\omega$ in equation (5), equation (6) is obtained:

$$Y_{ad-R-D}(j\omega) = \frac{1}{R_{ad}}(\cos(1.5\omega T_{sam}) - j\sin(1.5\omega T_{sam}))$$

$$\square \ \frac{1}{R_{CCF}} + \frac{1}{jX_{CCF}}$$

(6)

where R_{CCF} is the equivalent resistance, and X_{CCF} is the equivalent reactance, and are obtained as follows:

$$R_{CCF} = R_{ad} / \left(\cos\left(1.5\omega T_{sam}\right)\right)$$
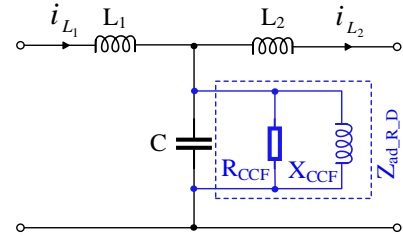$$X_{CCF} = R_{ad} / \left(\sin\left(1.5\omega T_{sam}\right)\right)$$

(7)

Figure 3. Equivalent virtual impedance due to CCF AD.

Both R_{CCF} and X_{CCF} parameters depend on the frequency. The border frequency of R_{CCF} is demonstrated by $f_{b,R-R}$ with both negative or positive values, where are specified as the border frequency the VPRR as well, and the border frequency of X_{CCF} is demonstrated by $f_{b,X-R}$ for capacitive or inductive mode. Based on equation (7), the border frequency of R_{CCF} can be considered as $f_{b,R-R} = f_{sam}/6$, and the border frequency of X_{CCF} can be considered $f_{b,X-R} = f_{sam}/3$. The equivalent resistance R_{CCF} in the range of $f < f_{sam}/6$ is positive, while it is negative for the $f > f_{sam}/6$ interval. The equivalent reactance X_{CCF} behaves as inductance for $f < f_{sam}/3$ interval, while it behaves as capacitor for $f > f_{sam}/3$ interval.

According to the standard of the Nyquist stability, the stability standard of the LCL-type grid-

tied inverter with digital control can be summarized in Table (1) [26], where P is the number of right half-plane poles (RHP) of the open loop transfer function, PM represents the phase margin and G_{Mf1} and G_{Mf2} are the phase margin at the LCL resonance frequency f_{res_LCL} and frequency of $f_{sam}/6$. The (-) subscript indicates a negative intersection with the phase of -180° and a further decrease in the phase angle after passing through -180˚, and a (+) subscript indicates a positive intersection with the phase of -180°, gives the increase of the phase angle after passing through the phase of -180˚ and $H_{i1,ref}$ can be expressed by equation (8).

$$H_{i1,ref} = \frac{L_1 \omega_{res\_LCL} \left[2\cos(\omega_{res\_LCL} T_{sam}) - 1 \right]}{\sin(\omega_{res\_LCL} T_{sam}) K_{PWM}} \qquad (8)$$

where ω_{res_LCL} is the resonance angular frequency of the LCL filter considering the network impedance and is written according to equation (9):

$$\omega_{res\_LCL} = 2\pi f_{res\_LCL} = \sqrt{\frac{L_1 + L_2 + L_g}{L_1(L_2 + L_g)C}} \qquad (9)$$

It is worth noting that the requirements of the gain margin (GM) for the second case ($H_{i1} > H_{i1,ref}$ and $f_{res\_LCL} < f_{sam}/6$) conflict with the fourth case ($f_{res\_LCL} > f_{sam}/6$). Because f_{res_LCL} decreases with the increase of L_g, if the variation of grid impedance L_g changes the range of the resonance frequency of the LCL filter f_{res_LCL} from $0 < f_{res\_LCL} < f_{sam}/6$ to $f_{res\_LCL} > f_{sam}/6$ and opposite, the inverter may become unstable. Furthermore, the stability of the inverter for $f_{res\_LCL} = f_{sam}/6$ is impossible. Thus, a region that is forbidden for the resonant frequency should be taken into account for f_{res_LCL} to approach $f_{sam}/6$, as indicated in Table (1) of [31].

3. LCL-type grid-tied system considering a phase compensator

3.1. Suggested Phase Compensator

As demonstrated in section two, if L_g has vast variations, f_{res_LCL} may change from $0 < f_{res\_LCL} < f_{sam}/6$ to the range of $f_{res\_LCL} > f_{sam}/6$ and

the opposite, resulting in system instability. The easiest route to deviate from this subject is to keep f_{res_LCL} below $f_{sam}/6$ without paying attention to L_g variations. However, the weight and volume of the LCL filter increase as a result of this issue, thereby reducing the power density. To adapt the grid-connected system to grid impedance changes more properly without increasing the size of the LCL filter, the chosen strategy is to attenuate the delay of digital control and increase the VPRR border frequency.
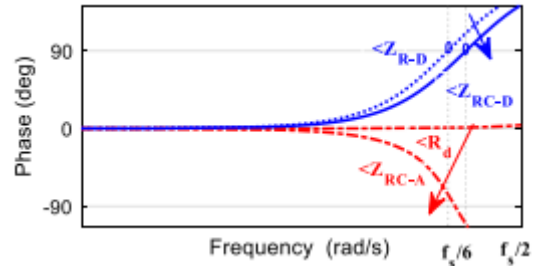

Figure 4. Phase diagram by frequency for $Z_{RC-D}(s)$, $Z_{R-D}(s)$, R_d, $Z_{RC-A}(s)$

Based on equation (5), the phase diagram in terms of frequency for R_{ad} and $Z_{ad-R-D}(s)$ can be depicted as Fig. 4. In this figure, $\angle Z_{ad-R-D}$ is equal to 90° in $f_{sam}/6$ frequency, which is equal to the VPRR border frequency as well. This point reveals that an increase in the border frequency is achieved when a phase delay is created in $Z_{ad-R-D}(s)$. In this situation, the modified virtual impedance phase angle creates an intersection at a higher frequency with an angle of 90˚. Considering this point, a virtual or unreal capacitor $C_{ad,p}$ is illustrated to be connected with R_{ad} in parallel to create the modified impedance Z_{ad-RC} according to Fig. 5(b), and $Z_{ad-RC}(s)$ is expressed according to equation (10).

$$Z_{ad-RC}(s) = R_{ad} \,\|\, \frac{1}{sC_{ad,p}} = \frac{R_{ad}}{1 + sR_{ad}C_{ad,p}} \qquad (10)$$

Table 1. Stability criterion for the LCL-type grid-tied inverter with CCF AD

parameters	1st case	2nd case	3rd case	4th case
$f_{res\text{-}LCL}$	$(0, f_{sw}/6)$	$(0, f_{sam}/6)$	$f_{res\text{-}LCL} = f_{sam}/6$	$(f_{sam}/6, +\infty)$
H_{i1}	$(0, H_{i1,ref}]$	$(H_{i1,ref}, +\infty)$	-	$(0, +\infty)$
P	0	2	2	2
-180˚ crossing freq.	$f_{res\text{-}LCL\,(-)}$	$f_{res\text{-}LCL\,(-)}, f_{sam}/6$	none	$f_{res\text{-}LCL\,(+)}, f_{sam}/6\,_{(-)}$
GM Req.	$GM_{f1} > 0\text{dB}$	$GM_{f1} > 0\text{dB}$ $GM_{f2} < 0\text{dB}$	unstable	$GM_1 > 0\text{dB}$ $GM_2 < 0\text{dB}$
PM Req.	$PM > 0$	$PM > 0$	unstable	$PM > 0$

According to the delay of digital control, the real equivalent of virtual or unreal impedance can be expressed according to equation (11):

$$Z_{ad-RC-D}(s) = Z_{ad-RC}(s)e^{1.5sT_{sam}} = \frac{R_{ad}}{1+sR_{ad}C_{ad,p}}e^{1.5sT_{sam}}$$

(11)

The phase diagram in terms of frequency for $Z_{ad-RC-D}(s)$ is shown in Fig. 4, using a solid and continuous line that $Z_{RC\_D}(s)$ intersects a 90° angle at a frequency more than $f_{sam}/6$. Hence, the cut-off frequency of the VPRR can be incremented by $Z_{ad-RC-D}(s)$.
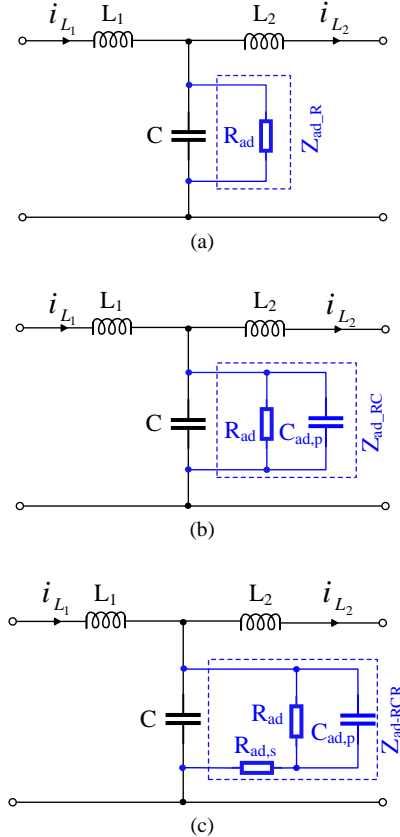

(a)

(b)

(c)

Figure 5. The change and evolution process of equivalent virtual or unreal impedance, (a). absolute resistance, (b). resistive-capacitive network, (c). resistive-capacitive-resistive network

The imaginary part of $Z_{ad-RC-D}(s)$, which can be considered as an admittance, can be expressed by the equation (12),

$$Y_{ad-RC-D}(s) = \frac{1}{Z_{ad-RC-D}(s)} = (1+sR_{ad}C_{ad,p}) \cdot \frac{e^{-1.5sT_{sam}}}{R_{ad}}$$

$$\square T_{com\_L}(s) \cdot \frac{1}{R_{ad}}e^{-1.5sT_{sam}}$$

(12)

where T_{com_L} is the transfer function of the first-order derivative compensator and is specified as (13).

$$T_{com\_L}(s) = 1+sR_{ad}C_{ad,p}$$

(13)

By comparing equation (12) with (5), the modified virtual and unreal impedance $Z_{ad-RC-D}(s)$ introduces $T_{com\_L}(s)$ equally in the path of the LCL filter's capacitor current feedback. This point can be seen in Fig. 6, assuming $G_c(s) = T_{com\_L}(s)$. It should be noted that the derivative compensator efficiently amplifies the noise with high frequency characteristics in the path of LCL filter's capacitor current feedback. To solve the mentioned issue, another virtual and unreal resistor R is proposed, which is connected with $Z_{ad-RC}(s)$ in series and forms Z_{ad-RC} according to Fig. 5(c), which is expressed by the following expression:

$$Z_{ad-RCR}(s) = Z_{ad-RC}(s) + R_{ad,s}$$
$$= \frac{(R_{ad}+R_{ad,s})+sR_{ad}R_{ad,s}C_{ad,p}}{1+sR_{ad}C_{ad,p}}$$

(14)

By replacing Z_{ad-RC} with Z_{ad-RCR} in equation (7), the real impedance equivalent of $Z_{ad-RCR-D}$ in the presence of digital control delay is obtained according to equation (15).

$$Z_{ad-RCR-D}(s) = Z_{ad-RCR}(s)e^{1.5sT_{sam}}$$
$$= \frac{(R_{ad}+R_{ad,s})+sR_{ad}R_{ad,s}C_{ad,p}}{1+sR_{ad}C_{ad,p}}e^{1.5sT_{sam}}$$

(15)

The admittance of $Z_{ad-RCR-D}$ can be expressed by equation (16), where $T_{com,LL}$ is the transfer function of the lead-lag compensator and is expressed as equation (17). According to equation (16), the admittance of $Z_{ad-RCR-D}(s)$ impedance can be understood by replacement of $G_c(s)$ compensator in Fig. 6 with $T_{com,LL}(s)$ compensator. It should be noted that the zero of $T_{com,LL}(s)$ should be considered precisely in the vicinity of f_{sam} to compensate for the phase delay raised from the digital control. For this purpose, in this paper, the zero of the transfer function of $T_{com,LL}(s)$, i.e. $(1/mT)$, is placed in $2f_{sam}$, and mT is set to $0.5T_{sam}$. Thus, $T_{com,LL}(s)$ is rewritten as equation (18).

$$Y_{ad-RCR-D}(s) = \frac{1+sR_{ad}C_{ad,p}}{(R_{ad}+R_{ad,s})+sR_{ad}R_{ad,s}C_{ad,p}}e^{-1.5sT_{sam}}$$

$$\square T_{com,LL}(s)\frac{1}{R_{ad}}e^{-1.5sT_{sam}}$$

(16)

$$T_{com,LL}(s) = \frac{R_{ad}}{R_{ad}+R_{ad,s}} \cdot \frac{1+sR_{ad}C_{ad,p}}{1+s \cdot \frac{R_{ad,s}}{R_{ad}+R_{ad,s}} \cdot R_{ad}C_{ad,p}} \quad (17)$$

$$\square A_{LL} \cdot \frac{1+mT_{sam}}{1+sT_{sam}}$$

$$T_{com,LL}(s) = A_{LL} \cdot \frac{1+0.5sT_{sam}}{1+s(0.5T_{sam}/m)} \quad (18)$$

It is worth mentioning that there is a pole in the transfer function of $T_{com,LL}(s)$. By correctly considering this pole, the unwanted noise occurred by the switching can be effectively decreased in the CCF path. Using bilinear transformation, the discrete form of $T_{com,LL}(s)$ is obtained by considering $s=2(z-1)/(T_s(z+1))$ in equation (18), which can be expressed by equation (19).

$$T_{com,LL}(z) = A_{LL} \cdot \frac{1+(m-1)/m+1}{1+(m-1)/(m+1).z^{-1}} \square A_{LL} \cdot \frac{1+n}{1+n.z^{-1}} \quad (19)$$

where the m and n parameters can be defined in the above equation as follows:

$$n = (m-1)/(m+1) \quad , \quad m \in (1,\infty) \quad (20)$$

So, the expression of the proposed phase compensator, namely $T_{com,LL}(z)$, is obtained.

3.2. Stability for Grid-tied Inverter by LCL Filter Considering Phase Compensation

Adding the phase compensator affects the stable performance of the LCL-type grid-tied inverter. This section analyses the stability and passivity criterion. Also, the advantages of the introduced phase compensator are demonstrated.

By substituting $z = e^{sT_{ams}}$ in equation (19), the introduced phase compensator in the s domain can be considered as follows:

$$T'_{com,LL}(s) = A_{LL} \cdot \frac{1+n}{1+n.e^{-sT_{sam}}} \quad , \quad n \in (0,1) \quad (21)$$

Replacing $T_{com,LL}(s)$ in relation (16) with $T'_{com,LL}$ leads to the following equation:

$$Y'_{ad-RCR-D}(s) = A_{LL} \cdot \frac{1+n}{1+n.e^{-sT_{sam}}} \cdot \frac{1}{R_{ad}} \cdot e^{-1.5sT_{sam}} \quad (22)$$

By substituting $s = j\omega$ in equation (22), equation (23) is obtained where $R_{ad-RCR-D}$ and $X_{ad-RCR-D}$ are equivalent resistance, and reactance, respectively, which are defined according to (24) and (25).

$$R_{ad-RCR-D} = \frac{R_{ad}}{A_{LL}} \cdot \frac{n^2+2n\cos(\omega T_{sam})+1}{(1+n)(\cos(1.5\omega T_{sam})+n\cos(0.5\omega T_{sam}))} \quad (24)$$

$$Y'_{ad-RCR-D}(s) = A_{LL} \cdot \frac{1+n}{1+n.e^{-sT_{sam}}} \cdot \frac{1}{R_{ad}} \cdot e^{-1.5sT_{sam}} \quad (25)$$

$f_{b,R-RCR}$ is defined as the border frequency of $R_{ad-RCR-D}$ virtual and unreal resistance, which may have a positive or negative value. Besides, $f_{b,X-RCR}$ is considered to be the border frequency of $X_{ad-RCR-D}$ virtual reactance, which can have inductive or capacitive behaviour. Assuming the truth of equation (26), equation (27) is obtained.

$$\begin{cases} \cos(1.5\omega T_{sam})+b\cos(0.5\omega T_{sam})=0 \\ \sin(1.5\omega T_{sam})+b\sin(0.5\omega T_{sam})=0 \end{cases} \quad (26)$$

$$\begin{cases} f_{b,R-RCR} = (\arccos((1-n)/2))(f_{sam}/2\pi) \\ f_{b,X-RCR} = (\pi-\arccos((1+n)/2))(f_{sam}/2\pi) \end{cases} \quad (27)$$

Since $0 < n < 1$, the border frequency of virtual and unreal resistance is in the range of $f_{sam}/6 < f_{b,R-RCR} < f_{sam}/4$, and the border frequency of virtual reactance is in the range of $f_{sam}/3 < f_{b,X-RCR} < f_{sam}/2$. Accordingly, both $f_{b,X-RCR}$ and $f_{b,R-RCR}$ border frequencies are more than $f_{b,R-R}$ and $f_{b,X-R}$ frequencies, which can be seen in the amplitude diagram in terms

$$Y'_{ad-RCR-D}(j\omega) = \frac{A_{LL}}{R_{ad}} \cdot \frac{1+n}{n^2+2n\cos(\omega T_{sam})+1} \cdot ((\cos(1.5\omega T_{sam})+n\cos(0.5\omega T_{sam})) - j(\sin(1.5\omega T_{sam})+n\sin(0.5\omega T_{sam})))$$

$$\square \frac{1}{R_{ad-RCR-D}} + \frac{1}{jX_{ad-RCR-D}} \quad (23)$$

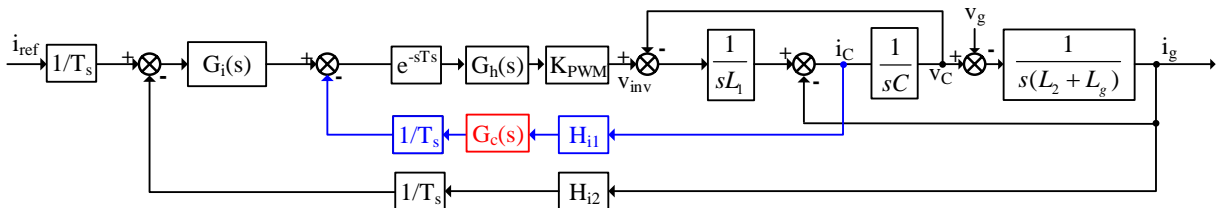
Figure 6. Control block diagram of LCL-type grid-connected inverter in the presence of phase compensator

$$GH_{RCR-D}(z) = \frac{G_i(z)H_{i2}K_{PWM}}{\omega_{res\_LCL}(L_1+L_2+L_g)(z-1)} \cdot \frac{\omega_{res\_LCL}T_{sam}(z^2-2z\cos(\omega_{res\_LCL}T_{sam})+1)-(z-1)^2\sin(\omega_{res\_LCL}T_{sam})}{z(z^2-2z\cos(\omega_{res\_LCL}T_s)+1)+(z-1)\cdot\dfrac{H_{i1}K_{PWM}}{\omega_{res\_LCL}L_1}\cdot\sin(\omega_{res\_LCL}T_{sam})\cdot T'_{com\_LCL}(z)}$$

(28)

$$z(z-1)(z^2-2z\cos(\omega_{res\_LCL}T_{sam})+1)+(z-1)^2\frac{K_{PWM}H_{i1}}{L_1\omega_{res\_LCL}}\cdot\sin(\omega_{res\_LCL}T_{sam})T'_{com\_LL}(z)=0 \quad (29)$$

of frequency for $R_{ad\text{-}RCR\text{-}D}$ virtual resistance and $X_{ad\text{-}RCR\text{-}D}$ virtual reactance in Fig. 7. Thus, the suggested phase compensation is acceptable for attenuating the delay of digital control and increasing the border frequency of VPRR.

The $GH_{RCR-D}(z)$ term is defined as the current loop gain or the open loop transfer function of the inverter in the presence of the introduced phase compensator in the z domain. According to Fig. 6, $GH_{RCR-D}(z)$ is considered as equation (28). The characteristic equation of the transfer function $GH_{RCR-D}(z)$ can be expressed according to (29).

The pole count of the closed-loop transfer function $GH_{RCR-D}(z)$ beyond the unit circle is specified by the count of right half-plane roots in the equivalent s domain of equation (29). For ease of analysis, equation (29) is transferred from the discrete domain to the continuous domain by substituting $z=(1+\omega).(1-\omega)^{-1}$, which results in equation (30).

$$n_0\omega^3+n_1\omega^2+n_2\omega+n_3=0 \quad (30)$$

which

$$\begin{cases} n_0=2(1-n)(1+\cos(\omega_{res\_LCL}T_{sam})) \\ \quad +\dfrac{2(1-n)K_{PWM}H'_{i1}}{L_1\omega_{res\_LCL}}\sin(\omega_{res\_LCL}T_{sam}) \\ n_1=2(1+n)(1+\cos(\omega_{res\_LCL}T_{sam})) \\ \quad -\dfrac{4(1+n)K_{PWM}H'_{i1}}{L_1\omega_{res\_LCL}}\sin(\omega_{r\_LCL}T_s) \\ n_2=2(1-n)(1-\cos(\omega_{res\_LCL}T_{sam})) \\ \quad +\dfrac{2(1+n)K_{PWM}H'_{i1}}{L_1\omega_{res\_LCL}}\sin(\omega_{res\_LCL}T_{sam}) \\ n_3=2(1+n)(1-\cos(\omega_{res\_LCL}T_{sam})) \end{cases} \quad (31)$$

$$H'_{i1} \square H_{i1}K_{LL} \quad (32)$$

The Routh array for equation (31) can be calculated as equation (33). According to the Routh stability criterion, the number of right half-plane roots in equation (29) is equal to the sign changes

count in the first column in the Routh array, that is, $[n_0, n_1, (n_1n_2 - n_0n_3)/n_1, n_3]^T$.
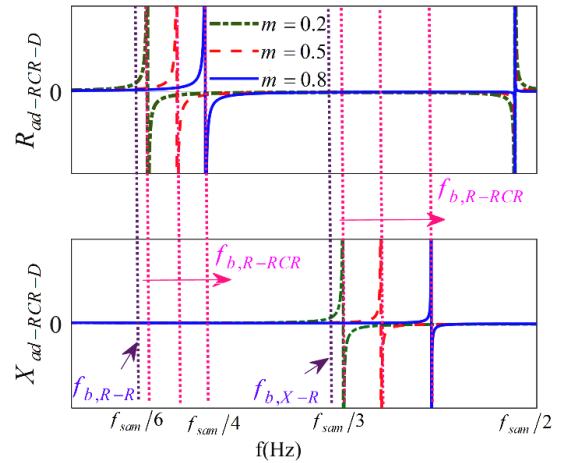

Figure 7. Amplitude diagram versus frequency for R_{RCR} and X_{RCR}

$$\begin{array}{lcc} \omega^3: & n_0 & n_2 \\ \omega^2: & n_1 & n_3 \\ \omega^1: & \dfrac{n_1n_2-n_0n_3}{n_1} & 0 \\ \omega^0: & n_3 & \end{array} \quad (33)$$

To ensure the system's controllability, the resonance frequency f_{res_LCL} must be less than $f_{sam}/2$, which leads to the $\omega_{res\_LCL}T_{sam} \leq \pi$ expression. Due to H_{i1} is assumed a positive value ($H_{i1} > 0$), and the expressions $sin(\omega_{res\_LCL}T_{sam}) > 0$, and $1-cos(\omega_{res\_LCL}T_{sam}) > 0$ are valid as well, the range of $n_0 > 0$, $n_2 > 0$ and $n_3 > 0$ will result for the Routh arrays elements based on equation (31). Thus, in equation (29), if $n_1 \leq 0$ or $(n_1n_2 - n_0n_3)/n_1 < 0$, there will be two sign variations in the first column of the Routh array, which indicates the presence of two roots in the right half-plane. If $n_1 \leq 0$, we have:

$$H'_{i1} \geq \frac{(1+\cos(\omega_{res\_LCL}T_s))\omega_{r\_LCL}L_1}{2K_{PWM}\sin(\omega_{res\_LCL}T_s)} \quad (34)$$

Now if $(n_1n_2 - n_0n_3)/n_1 < 0$, we have:

$$\begin{cases} H'_{i1} > \dfrac{L_1\omega_{res\_LCL}\left[2\cos(\omega_{res\_LCL}T_{sam})+n-1\right]}{(n+1)\sin(\omega_{res\_LCL}T_{sam})K_{PWM}} \\[2em] H'_{i1} < \dfrac{L_1\omega_{res\_LCL}\left[1+\cos(\omega_{res\_LCL}T_{sam})\right]}{2\sin(\omega_{res\_LCL}T_{sam})K_{PWM}} \end{cases} \quad (35)$$

Hence, in the condition that inequality (36) is true, $GH_{RCR-D}(z)$ contains two poles of the closed loop transfer function beyond the unit circle:

$$H'_{i1} > \frac{(2\cos(\omega_{res\_LCL}T_s)+b-1)\omega_{res\_LCL}L_1}{(b+1)K_{PWM}\sin(\omega_{res\_LCL}T_s)} \square H_{i1C} \quad (36)$$

It should be noted that H_{i1C} is positive in the $f_{res\_LCL} < f_{b,R\text{-}RCR}$ frequency range and negative in the $f_{res\_LCL} > f_{b,R\text{-}RCR}$ frequency range.

By replacing $H'_{i1} = H_{i1C}$ in equation (28), the $z_{1,2} = \cos(2\pi f_{b,R-RCR}T_{sam}) \pm j\sin(2\pi f_{b,R-RCR}T_{sam})$ expression is obtained, which expresses the resonance frequency of the current loop gain (f_{res_T}). In other words, for $H'_{i1}=H_{i1C}$ ($H_{i1C} > 0$), the resonance frequency of the current loop gain f_{res_T} is exactly equal to $f_{b,R\text{-}RCR}$. Using the equation (28), the bode diagram of the open loop transfer function $GH_{RCR-D}(s)$ can be drawn for the conditions of $f_{res\_LCL} < f_{b,R\text{-}RCR}$, and $f_{res\_LCL} \geq f_{b,R\text{-}RCR}$ in Figs. 8(a) and 8(b), respectively. In these figures, the value of H'_{i1} increases in the graphs with bigger label numbers. According to Fig. 8, the following expressions can be stated:

1. For $f_{res\_LCL} < f_{b,R\text{-}RCR}$ and $H'_{i1} \leq H_{i1C}$, the phase diagram in terms of frequency for $GH_{RCR-D}(s)$ has only one negative intersection with the phase of -180° at f_1 frequency, according to curves numbered 1, 2, and 3 in Fig. 8(a).

2. For $f_{res\_LCL} < f_{b,R\text{-}RCR}$ and $H'_{i1} > H_{i1C}$, the phase diagram in terms of frequency for $GH_{RCR-D}(s)$ has a negative intersection with the phase of -180° at the f_1 frequency and a positive intersection with the -180° at f_2 frequency, according to curve 4 of Fig. 8(a).

For $f_{res\_LCL} \geq f_{b,R\text{-}RCR}$, the phase diagram in terms of frequency for $GH_{RCR-D}(s)$ has a negative intersection with the phase of -180° at f_1 frequency and a positive intersection with the phase of -180° in the f_2 frequency, according to curves numbered 1, 2, and 3 in Fig. 8(b).

Considering $\omega = \omega_{res\_LCL} = 2\pi f_{res\_LCL}$ and $\omega = \omega_{Rb} = 2\pi f_{b,R\text{-}RCR}$ in equation (28), equations (37) and (38) are obtained, where $\angle T'_{com\_LL}(j\omega_{res\_LCL})$ and $\angle T'_{com\_LL}(j\omega_{b,R})$ are the phase angles of $T'_{com\_LL}(s)$ transfer function at resonance frequency f_{res_LCL} and border frequency $f_{b,R\text{-}RCR}$, successively It will be

depicted that $\angle T'_{com\_LL}(j\omega)$ lies in the (0, π/4) range in section 4.a. Therefore, the phase angle of transfer function $GH_{RCR-D}(s)$ is less than -180° at f_{res_LCL} and $f_{b,R\text{-}RCR}$ frequencies. Therefore, the equation (39) is obtained. For this reason, according to Table (2), the criterion of stability in $f_{res\_LCL} < f_{b,R\text{-}RCR}$ and $H'_{i1} > H_{i1C}$ conditions could be considered integrated with the stability benchmark in the $f_{res\_LCL} \geq f_{b,R\text{-}RC}$ condition. Compared to Table (1), the prohibited region of LCL filter resonance frequency is removed. This significant feature leads to the robust performance of the inverter against broad variations in network impedance.
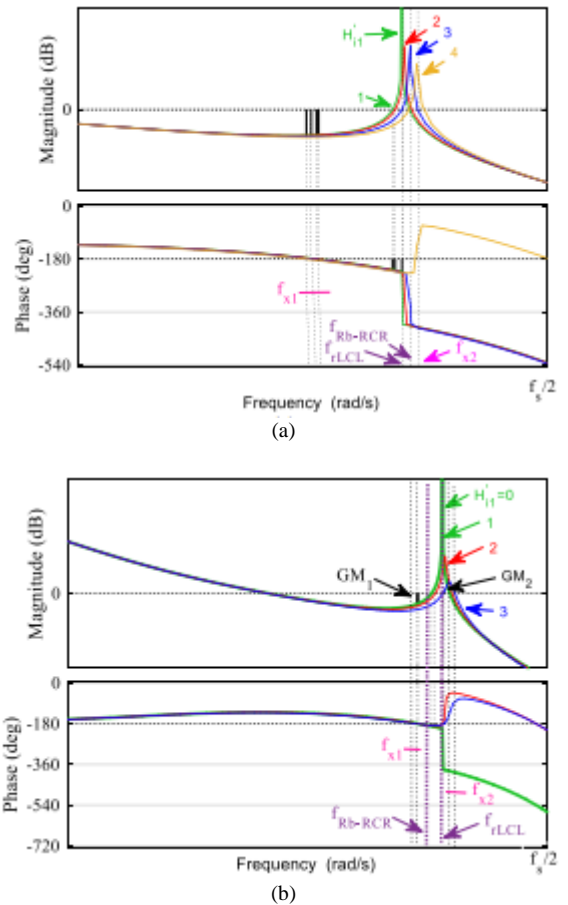

(a)

(b)

Figure 8. Bode diagram of the current loop gain;
(a). $f_{res\_LCL} < f_{Rb\_RCR}$, (b). $f_{res\_LCL} \geq f_{Rb\_RCR}$

To summarize the aforementioned topics, the suggested phase compensator can be effective in improving the performance of the LCL-type grid-connected inverter from the following perspectives:

The phase compensator is simple, easy to understand, and robust to the noise of the switching frequency apart from modifying the

$$GH_{RCR-D}(e^{j\omega_{res\_LCL}T_{sam}}) = \frac{K_p H_{i2}}{H'_{i1}} \cdot \frac{L_1}{L_1+L_2+L_g} \cdot \frac{\sqrt{n^2+2n\cos(\omega_{res\_LCL}T_{sam})+1}}{(1+n)}\exp(-j(\pi+\angle T'_{com\_LL}(j\omega_{res\_LCL})))$$

(37)

$$GH_{RCR-D}(e^{j\omega_{b,R}T_{sam}}) = \begin{cases} \dfrac{K_p H_{i2}}{|H'_{i1}-H_{i1C}|}\cdot\dfrac{L_1-K_{PWM}H_{i1C}T_{sam}}{L_1+L_2+L_g}\cdot\dfrac{1}{\sqrt{n+1}}\exp(-j(\pi+\angle T'_{com\_LL}(j\omega_{b,R}))) & H'_{i1}>H_{i1C} \\[4mm] \dfrac{K_p H_{i2}}{|H'_{i1}-H_{i1C}|}\cdot\dfrac{L_1-K_{PWM}H_{i1C}T_{sam}}{L_1+L_2+L_g}\cdot\dfrac{1}{\sqrt{n+1}}\exp(-j(2\pi+\angle T'_{com\_LL}(j\omega_{b,R}))) & H'_{i1}<H_{i1C} \end{cases}$$

(38)

$$\begin{cases} f_{x1} < \min(f_{r\_LCL}, f_{Rb\_RCR}) \\ f_{x2} > \max(f_{r\_LCL}, f_{Rb\_LCL}) \end{cases}$$

(39)

Table 2: Stability benchmark for phase-compensated grid-tied inverter

parameters	1st case	2nd case	3rd case
$f_{r\text{-}LCL}$	$f_{r\text{-}LCL} < f_{Rb\text{-}RCR}$	$f_{r\text{-}LCL} < f_{Rb\text{-}RCR}$	$f_{r\text{-}LCL} \geq f_{Rb\text{-}RCR}$
H'_{i1}	$(0, H_{i1C}]$	$(H_{i1C}, +\infty)$	$(0, +\infty)$
P	0	2	2
-180˚ crossing freq.	$f_{x1\,(-)}$	$f_{x1\,(-)}, f_{x2\,(+)}$	$f_{x1\,(-)}, f_{x2\,(+)}$
GM Req.	$GM_1 > 0dB$	$GM_1 > 0dB$ $GM_2 < 0dB$	$GM_1 > 0dB$ $GM_2 < 0dB$
PM Req.	$PM > 0$	$PM > 0$	$PM > 0$
$f_{r\text{-}T}$	$f_{r\text{-}T} \leq f_{Rb\text{-}RCR}$	$f_{r\text{-}T} > f_{Rb\text{-}RCR}$	$f_{r\text{-}T} > f_{Rb\text{-}RCR}$
Typical Curves	Curves 2 & 3 in Fig 8(a)	Curve 4 in Fig 8(a)	Curves 2 & 3 in Fig 8(b)

modulation index.

- The suggested phase compensation increases the VPRR's border frequency and suitably compensates the delay of digital control.

The suggested phase compensation removes the prohibited region of LCL filter resonance frequency and improves the robust performance of the inverter against broad variations of network impedance.

4. Design of LCL-type grid-connected inverter considering phase compensator

The mathematical model of the grid-connected inverter system is changed by adding the proposed phase compensator. To ensure the stability as well as proper operation of the control system, this section begins with a detailed method to design of the current regulator, phase compensator, and capacitor current feedback coefficient. Then, an example is presented to express the design method.

4.1. Phase Compensator Design

The purpose of the phase compensator is to alleviate the effects of the phase delay caused by the digital control delay. According to equation (21), the two main coefficients of the phase compensator are A_{LL} and n. According to equation (32), A_{LL} can be expressed in a way in the CCF coefficient, which will be mentioned in the next section. Hence, the

main focus in this section is mainly on designing the amount of n.

The phase of $T'_{com,LL}(j\omega)$ can be expressed according to the equation (40).

$$\angle T'_{com,LL}(j\omega) = \arccos\frac{1+n\cos(\omega T_{sam})}{\sqrt{n^2+2n\cos(\omega T_{sam})+1}}$$

(40)

By rewriting equation (40), the following equation is obtained:

$$\cos\angle T'_{com,LL}(j\omega) = \frac{1+n\cos(\omega T_{sam})}{\sqrt{n^2+2n\cos(\omega T_{sam})+1}} \quad , n\in(0,1)$$

$$= \frac{|(\cos(\omega T_{sam})+j\sin(\omega T_{sam}))-(-n)|^2+|1|^2-|-n|^2}{2|(\cos(\omega T_{sam})+j\sin(\omega T_{sam})-(-n)|\cdot|1|}$$

(41)

Based on the equation (41), it is possible to draw the $T'_{com,LL}(j\omega)$ graph as shown in Fig. 9 in the complex plane. According to this figure, for a particular value of b, when ωT_{sam} is close to zero or π, $T'_{com,LL}(j\omega)$ is almost equal to zero. But it reaches its peak value for $\omega T_{sam}=\pi/2$. Meanwhile, the peak value of $T'_{com,LL}(j\omega)$ enlarges with the b increase in the range of allowed variations.

Accordingly, if n is close to the unit value, an utmost phase angle compensation of about 45˚ can be created by the phase compensator. According to
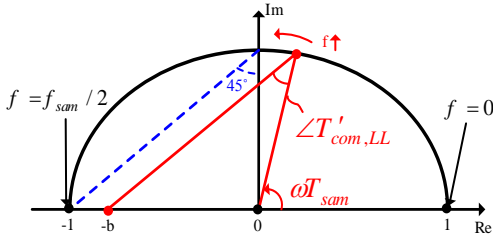
Figure 9. Diagram with frequency changes

Fig 9, equation (42) can be expressed:

$$\angle T'_{com,LL}(j\omega) \in (0, \pi/4) \tag{42}$$

As mentioned in Section 3.2, the discussed phase compensator can remove the forbidden range of LCL filter resonance frequency. Since both values of $\angle GH_{RCR-D}(j\omega_{res\_LCL})$ and $\angle GH_{RCR-D}(j\omega_{b,R})$ are less than -180°, the required GM for the open loop transfer function at f_1 and f_2 frequencies is not related to the sequence of resonance frequency f_{res_LCL} and border frequency $f_{b,R-RCR}$. To achieve sufficient phase margin and suitable phase difference of -180° in $\angle GH_{RCR-D}(j\omega_{res\_LCL})$ and $\angle GH_{RCR-D}(j\omega_{Rb})$, and besides compromise between the phase delay amount by preventing the noise transmission in the control system, the value of $\angle T'_{com,LL}(j\omega)$ greater than 10° is recommended. Thus, the $0.2 < n < 1$ range would be suitable. In this paper, the value of n is considered 0.8.

4.2. Determination of Current Compensator and Coefficient of CCF

Wide variations in network impedance have a large effect on the characteristics of the current open-loop transfer function. The regulator of the current and the feedback coefficient of the capacitor current should be designed in such a way that the

stable operation of the grid-tied inverter is maintained in the range of impedance variations. Considering this issue, a detailed design method for the current regulator parameters and feedback coefficient of the capacitor current is presented. The open-loop transfer function for the current control in the s domain based on Fig. 6 can be expressed as equation (43), where in this equation, $G_i(s)$ is the transfer function of the current regulator, which is considered a proportional-integral controller. The calculation and extraction procedure of the crossover frequency f_c, phase margin, regulator coefficients, gain of open-loop transfer function at the fundamental frequency T_{fo} is illustrated in [33]. The phase margin PM can be expressed according to equation (44) after replacing K_p and K_i in the main expression, in which $D(\omega)$ and $E(\omega)$ are considered as follows:

$$\begin{cases} D(\omega) = \dfrac{n\cos(0.5\omega T_{sam}) + \cos(1.5\omega T_{sam})}{n^2 + 2n\cos(\omega T_{sam}) + 1} \\[4mm] E(\omega) = \dfrac{n\sin(0.5\omega T_{sam}) + \sin(1.5\omega T_{sam})}{n^2 + 2n\cos(\omega T_{sam}) + 1} \end{cases} \tag{45}$$

The coefficient of H'_{i1} can be caught as equation (46). As mentioned in Table 2, the open loop transfer function should have a sufficient gain margin in f_1 and f_2 frequencies. So, relations (47) and (48) can be written.

$$\begin{cases} \angle G_{ad-RCR}(j\,2\pi f_1) = -180° \\ GM_1 = -20\lg\left|G_{ad-RCR}(j\,2\pi f_1)\right| \end{cases} \tag{47}$$

$$\begin{cases} \angle G_{ad-RCR}(j\,2\pi f_{x2}) = -180° \\ GM_2 = -20\lg\left|G_{ad-RCR}(j\,2\pi f_{x2})\right| \end{cases} \tag{48}$$

$$G_{ad-RCR}(s) = \frac{K_{PWM}H_{i2}}{L_1(L_2+L_g)C} \cdot \frac{e^{-1.5sT_{sam}}}{s\left(s^2 + s\cdot\dfrac{K_{PWM}H'_{i1}}{L_1}e^{-1.5sT_{sam}}\cdot\dfrac{1+n}{1+ne^{-sT_{sam}}} + \omega^2_{res\_LCL}\right)} \cdot G_i(s) \tag{43}$$

$$PM = \frac{\pi}{2} - 3\pi f_c T_{sam} - \arctan\frac{K_i}{2\pi f_c K_p} - \arctan\frac{2\pi f_c K_{PWM}H'_{i1}(1+n)D(\omega_c)}{4\pi^2(f^2_{res\_LCL}-f^2_c)L_1 + 2\pi f_c K_{PWM}H'_{i1}(1+n)E(\omega_c)} \tag{44}$$

$$H'_{i1\_PM} = \frac{2\pi L_1}{(1+n)K_{PWM}f_c} \cdot \frac{(f^2_{res\_LCL}-f^2_c)[f^2_c - f_o\sqrt{10^{\frac{T_{fo}}{10}}\cdot f^2_o - f^2_c}\tan(3\pi f_c T_{sam}+PM)]}{D(\omega_c)\left[f^2_c\tan(3\pi f_c T_{sam}+PM)+f_o\sqrt{10^{\frac{T_{fo}}{10}}\cdot f^2_o - f^2_c}\right] - E(\omega_c)\left[f^2_c - f_o\sqrt{10^{\frac{T_{fo}}{10}}\cdot f^2_o - f^2_c}\tan(3\pi f_c T_{sam}+PM)\right]} \tag{46}$$

$$\begin{cases} H'_{i1}(f_1,GM_1,f_c) = \dfrac{2\pi(f^2_{res\_LCL}-f_1^2)L_1}{(1+n)K_{PWM}f_1\left[D(\omega_1)\tan(3\pi f_1 T_{sam})-E(\omega_1)\right]} \\[4mm] H'_{i1}(f_1,GM_1,f_c) = \dfrac{2\pi L_1}{(1+n)K_{PWM}f_1}\left[(f_1^2-f^2_{res\_LCL})E_N(\omega_1)+A\right] \end{cases} \qquad (49)$$

$$\begin{cases} H'_{i1}(f_{x2},GM_2,f_c) = \dfrac{2\pi(f^2_{res\_LCL}-f_2^2)L_1}{(1+n)K_{PWM}f_2\left[D(\omega_1)\tan(3\pi f_2 T_{sam})-E(\omega_1)\right]} \\[4mm] H'_{i1}(f_{x2},GM_2,f_c) = \dfrac{2\pi L_1}{(1+n)K_{PWM}f_2}\left[(f_2^2-f^2_{res\_LCL})E_N(\omega_1)+A\right] \end{cases} \qquad (50)$$

$$A = \sqrt{\left(f^2_{res\_LCL}10^{\frac{GM_1}{20}}\cdot\frac{f_c}{f_1}\right)^2\left\{\left[\cos(2\pi f_1 T_s)+n\right]^2+\sin^2(2\pi f_1 T_{sam})\right\}-\left[\left(f_1^2-f^2_{res\_LCL}\right)D_N(\omega_1)\right]^2}$$

By substituting equation (43) in equations (47) and (48), equations (49) and (50) are obtained, which $D_N(\omega_1)$ is the fractional expressions of $D(\omega_1)$ and $E_N(\omega_1)$ is the fractional expressions of $E(\omega_1)$. It is worth noting that the frequency f_{res_LCL} depends on grid inductance L_g. Given that the equations (46), (49), and (50) are dependent on the f_{res_LCL}. H'_{i1} will naturally depend on grid inductance L_g. The important issue in the determination of H'_{i1} is to detect a suitable range that fulfills the specifications of GM_1, GM_2, and PM throughout the whole range of grid inductance variations [33].

The proportional-integral regulator whose coefficients were utilized in equation (44) is expressed as follows:

$$G_i(s) = K_p + K_i/s \qquad (51)$$

The amplitude of the open-loop transfer function or current loop gain at the gain crossover frequency f_c is equal to one:

$$\left|G_{ad-RCR}(j\,2\pi f_c)\right| = 1 \qquad (52)$$

By inserting the equation (43) and (51) in the equation (52), K_p is obtained based on the equation (53):

$$K_p \approx \frac{2\pi f_c(L_1+L_2+L_g)}{K_{PWM}H_{i2}} \qquad (53)$$

By defining T_{fo} as the gain of the at the fundamental frequency f_o and substituting $s = 2\pi f_o$ in equation (43), equation (54) is obtained:

$$T_{fo} = 20\lg\left|G_{RCR}(j\,2\pi f_o)\right| = 20\lg\left|\frac{H_{i2}K_{PWM}(K_p+K_i/j\,2\pi f_o)}{j\,2\pi f_o(L_1+L_2+L_g)}\right| \qquad (54)$$

By inserting (53) into (54), K_i is obtained based on the equation (55):

$$K_i \approx \frac{4\pi^2 f_o(L_1+L_2+L_g)}{H_{i2}K_{PWM}}\sqrt{(10^{\frac{T_{fo}}{20}}\cdot f_o)^2-f_c^2} \qquad (55)$$

The phase margin PM is calculated at the gain crossover frequency f_c. Therefore, according to equation (43), the quantity of PM is expressed as the following equation:

$$PM = 180° + \angle G_{ad-RCR}(j\,2\pi f_c) \qquad (56)$$

4.3. Design Example

To better understand the design method presented in Section 4.2, the design process is illustrated with an example. The primary parameters of the grid-connected inverter by LCL filter are illustrated in Table 3. Based on the determination method presented in section 4.2, the suitable gain margin, phase margin, and steady-state error are considered as $PM > 35°$, $T_{fo} > 50$dB, $GM_1 > 3$dB, and $GM_2 < -3$. According to the assumed values of Table 3, the frequency of f_{res_LCL} is considered as $8.7\ kHz$ for $L_g = 0$. Thus, the initial crossover frequency f_c is considered $2\ kHz$. Based on equations (53) and (55), $K_p = 0.84$ and $K_i = 2040$. Hence, $G_i(s)=0.84+2040/s$. In the next step, H'_{i1} can be obtained in terms of variable L_g using equations (46), (49), and (50). According to the calculated value for the CCF coefficient, it can be seen that H'_{i1} varies between 0.06 and 0.064. In this paper, the value of the CCF coefficient is selected as $H'_{i1} = 0.061$. It should be noted that all the ranges are unacceptable for H'_{i1}, the gain crossover frequency f_c should be reduced and steps 2 and 3 should be repeated until a suitable range is achieved.

Using the parameters obtained in Table 3, the zero-pole diagram of the current control closed-loop transfer function is shown in Fig. 10 (a) and (b) with

Table 3: The main parameters of the single-phase grid-connected inverter with the LCL filter

Parameter	Symbol	Value	Parameter	Symbol	Value
grid voltage	V_g	220 V	inverter side inductor	L_1	860 µH
output power	P_o	6 kW	Grid side inductor	L_2	95 µH
fundamental frequency	f_o	50 Hz	filter capacitor	C	7 µf
switching frequency	f_{sw}	15 kHz	DC link capacitor	C_{DC}	4700 µf
resonance frequency	f_{res}	5 kHz	triangular wave amplitude	V_{tri}	3 V
sampling frequency	f_{sam}	30 kHz	grid current sensor coefficient	H_{i2}	0.15
Lead compensator parameter	b	0.8	capacitor current sensor coefficient	H'_{i1}	0.062

(a)

(b)
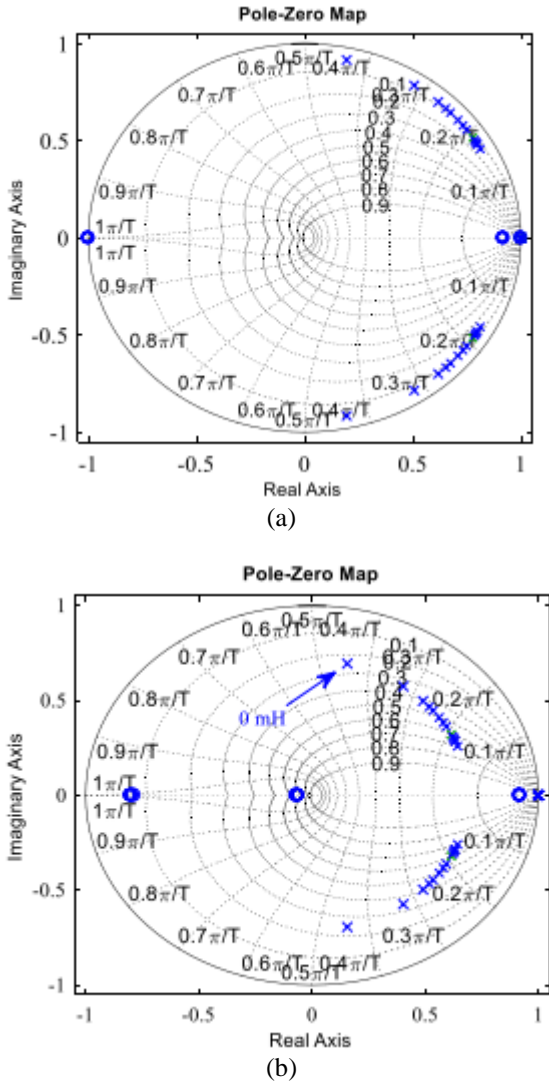
Figure 10. Zero-pole diagram of the closed-loop current control against network impedance changes, (a) without compensation, (b) with compensation

and without the phase compensation, respectively. Without phase compensation, for the range of 255 $\mu H < L_g < 600 \ \mu H$, the poles of the closed-loop current control with CCF active damping are located near the border of the unit circle as displayed in Fig. 10(a). On the contrary, utilizing phase compensator, all the poles of the closed-loop current control are located inside the unit circle according to Fig. 10(b), and far from the border of the unit circle.

Therefore, the grid-connected inverter has a stable performance in the range of grid inductance changes, which illustrates the possibility of implementing the introduced parameter determination method as well as the efficiency of the introduced phase compensation for passive and robust performance for wide grid inductance changes.

Fig. 11 displays the Bode diagram for the open loop transfer function in terms of grid inductance L_g. Without phase compensation and for $L_g = 255 \ \mu H$, the frequency f_{res_LCL} is exactly equal to $f_{sam}/6$, and its value is reduced to 5 kHz. Hence, the stability of
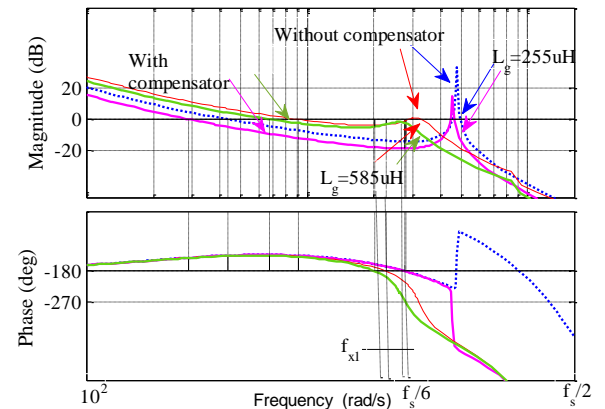

Figure 11. The bode diagram of open loop transfer function according to various network inductance in the presence of phase compensation

4

the inverter cannot be achieved. By increasing the grid inductance to 580 μH, the resonance frequency f_{res_LCL} decreases to *1.4 kHz*. However, the resonance frequency f_{res_LCL} is fewer than $f_{sam}/6$, it is in the prohibited range of resonance frequency. So, the inverter is unstable due to the inappropriate stability margin. Considering the introduced phase compensation, the prohibited area of the resonance frequency is removed, and as a result, the inverter works stably.

4.4. Sensitivity Analysis Against LCL Filter Parameter Changes

Sensitivity analysis and investigating the system stability against the changes of passive elements of the LCL filter is of particular importance. To analyze the system sensitivity to LCL filter parameter changes, which are defined by $C+\Delta C$, $L_1+\Delta L_1$, and $L_2+\Delta L_2$, besides the stability investigation of the grid-connected system, each parameter of the LCL filter has decreased by 5%, 10%, and 15%, respectively.

Fig. 12 demonstrates the effect of these changes on the stability of the closed-loop system with the proposed phase compensator. Fig. 12(a) displays the case where only the filter inductors have been changed. It is clear that the system is stable in this case and is not sensitive to changes in LCL filter inductors. In Fig. 12(b), only the filter capacitor is changed, and other parameters remain constant. In this case, similar to the previous case, the system has maintained its stability. Fig. 12(c) illustrates the case where the inductors and capacitors of the LCL filter are changed simultaneously. In this case, the system is stable and does not have considerable sensitivity to simultaneous changes of inductors and capacitors.

Changing the values of the LCL filter parameters affects the THD of the network injected current and the stability behavior. Table 4 demonstrates the results related to LCL filter parameters changing and their effect on the THD of the network injected current. According to Table 4, it can be concluded that the THD of the network injected current increases when the LCL filter inductors are more changed. In contrast, more changes in the LCL filter capacitor do not affect the THD value and can be ignored. Now, for the simultaneous changes of 5%, 10%, and 15% in inductors and capacitors of the LCL filter, the THD of the network injected current increases by 5.68%, 8.8%, and 14.20%.

Table 4: The THD value of the network injected current for the changes in the LCL filter

Parameter	Percentage for variations	THD (%)
L_1, L_2	5%	1.83
	10%	1.92
	15%	2.01
C	5%	1.74
	10%	1.73
	15%	1.78
L_1, L_2, C	5%	1.86
	10%	1.93
	15%	2.01

5. SIMULATION RESULTS

In this section, the simulation results related to fuel cell power transfer to a weak grid through an LCL-type grid-tied inverter are presented. The simulated fuel cell is of PEMFC type with a rated power of 6 kW and rated voltage of 45 V. To model the above conditions and confirm the correctness of the control system performance, the worst-case network impedance i.e., pure inductive with the value of 2.6 *mH* is considered, and the results of the conditions where the network impedance is 0 mH are presented as well. The fuel cell injected power into the network is sensitive to changes in the fuel flow rate. To investigate the stability of the system to changes in the fuel flow rate, this parameter was reduced by 20% in the time interval of [1,1.5] seconds and then returned to the previous amount.

The current-power and voltage-current curves of the fuel cell are shown in Figures 13(a) and (b), respectively. As shown in Fig. 13(a), with the increase in current, the power produced by the fuel cell also increases.

Fig. 14 displays the fuel flow rate, current, and voltage produced by the 6 kW PEMFC. To apply a 20% reduction in the generated power of the fuel cell and analyze the performance of the fuel cell grid-connected power conditioning system, the fuel flow rate has decreased by 20% in the time interval of [1,1.5] according to Fig. 14(a). As a result, the current produced by the fuel cell has decreased by about 10%, that is, from about 116 A to about 10 A. The voltage generated by the fuel cell is shown in Fig. 14(c). By reducing the fuel flow rate, the produced voltage of the PEMFC has decreased by about 12% and has reached from 53 V to 46.5 V. The decrease in voltage and produced current of the PEMFC has led to a decrease of about 20% of its

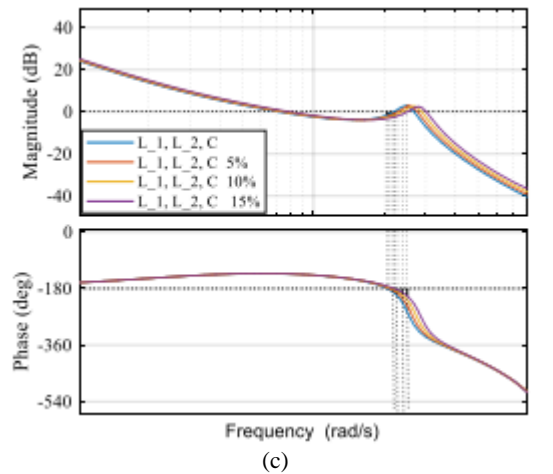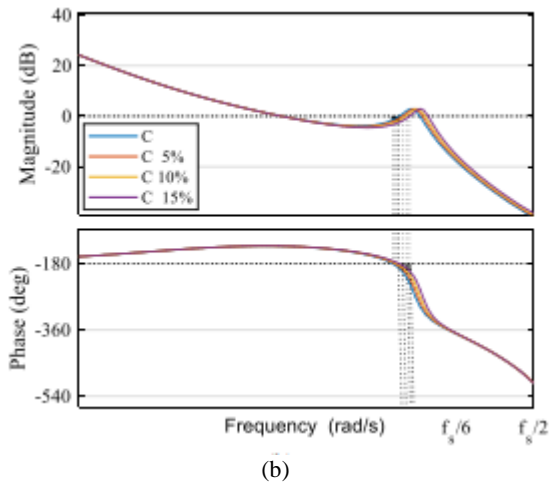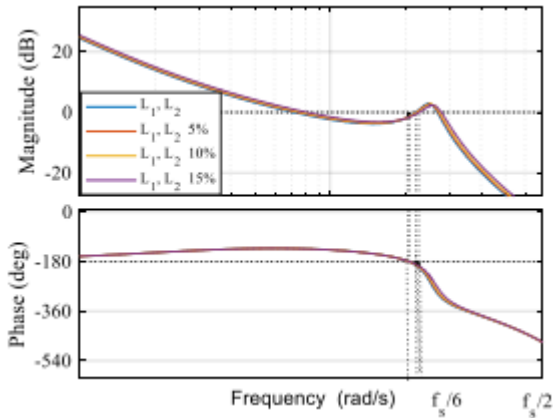produced power. The voltage produced by the fuel cell has low amplitude, according to Fig. 14(c).

(b) changing the LCL filter capacitor, (c) simultaneous change of inductors and capacitor of LCL filter

(a)

(b)

(c)

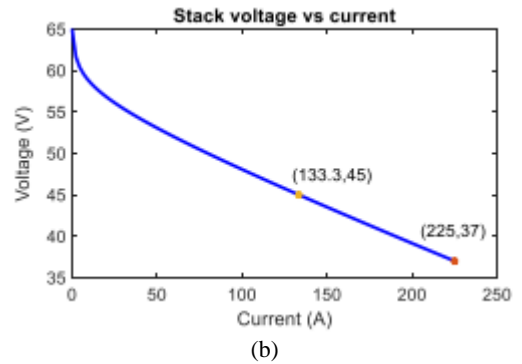Figure 12. Bode diagram of the closed-loop system with phase compensator, (a) changing the LCL filter inductors,

(a)

(b)
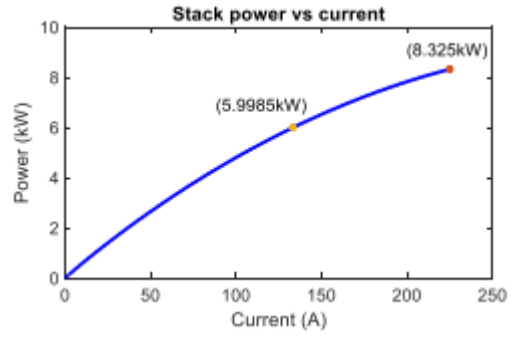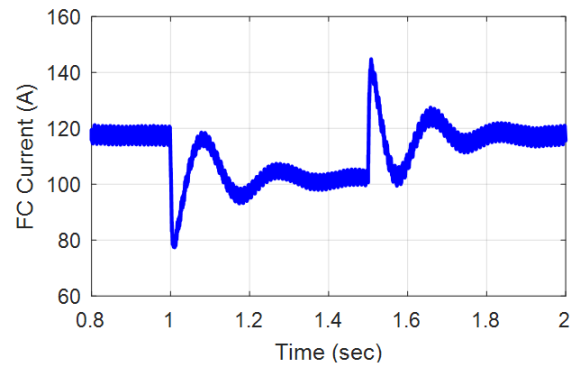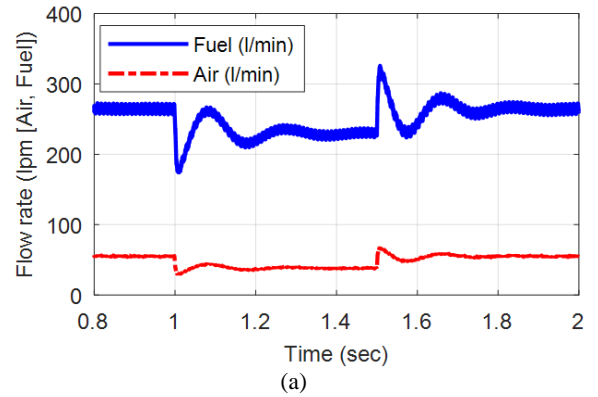
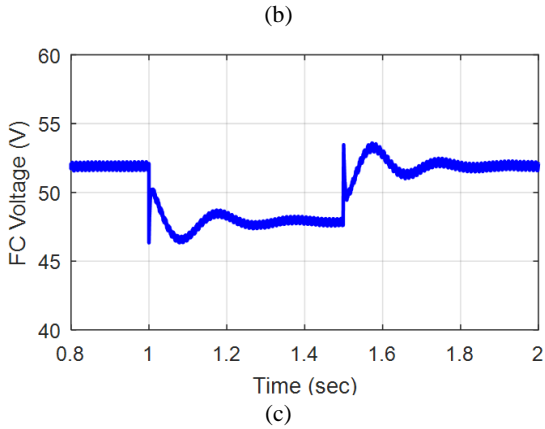Figure 13. PEMFC characteristic curves, (a) P-I, (b) V-I

(a)

(b)

(c)

Figure 14. (a) fuel and air flow rate, (b) current produced by the PEMFC, (c) voltage produced by the PEMFC

To adapt the generated voltage of the PEMFC to the requirements of the power grid, a boost converter is utilized to increase the PEMFC-generated voltage amplitude. The DC link voltage of the inverter, which is the output voltage of the boost converter, is shown in Fig. 15, along with the output voltage of the inverter. According to Fig. 15(a), it is clear that the DC link voltage is close to its reference value, which is set at 355 V, and the DC link voltage ripple

(a)

(b)

Figure 15. (a) DC link voltage or boost converter output voltage, (b) inverter output voltage
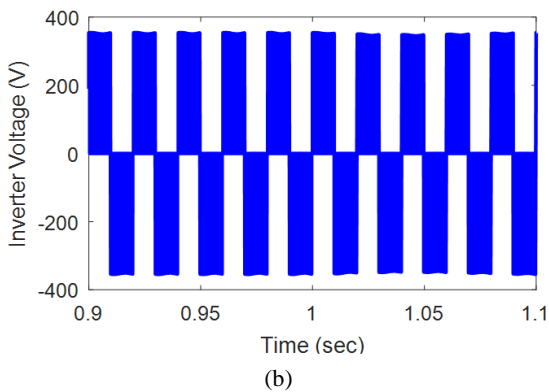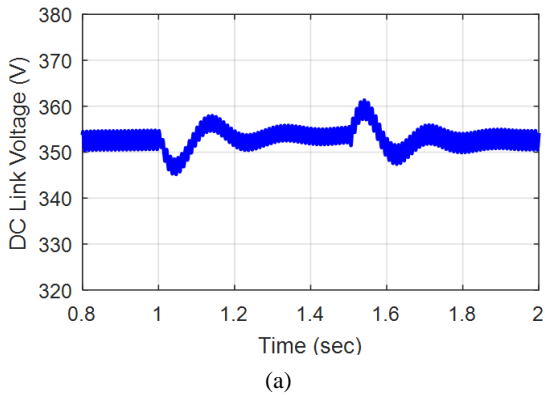
is very low. It is also clear that in the [1,1.5] time interval, the DC link voltage changes are tiny, and the DC link voltage controller works well. Fig. 15(b) displays the output voltage of the grid-tied inverter. The unipolar sinusoidal pulse width modulation (SPWM) is considered the switching method for the inverter. According to the low ripple of the DC link voltage, the output voltage of the inverter shows a suitable and unchanged range as well.

The generated power of the PEMFC as well as the injected power into the network by the grid-tied fuel cell power conditioning system are shown in Fig. 16. According to this figure, the PEMFC produces the power of about 6100 W, which decreases to about 4900 W when the fuel flow declines. The injected power of the system under study to the network in nominal conditions is about 5950 W, which has reached 4800 W with the reduction of the fuel flow. The fuel cells have a slower dynamic response compared to the solar arrays. Therefore, with the change in the fuel flow, it takes some time to reach a new stable condition. Of course, these fluctuations are not observed in the power injected into the network. The DC link capacitor acts as an interface between the fuel cell
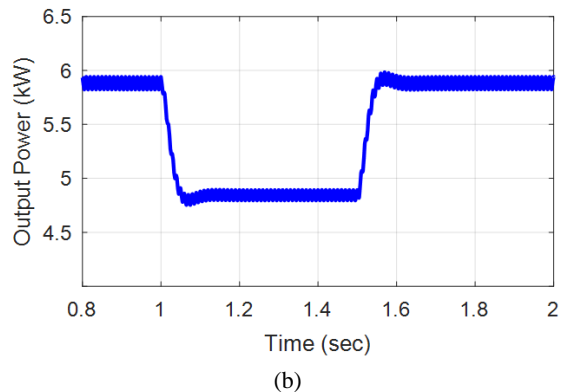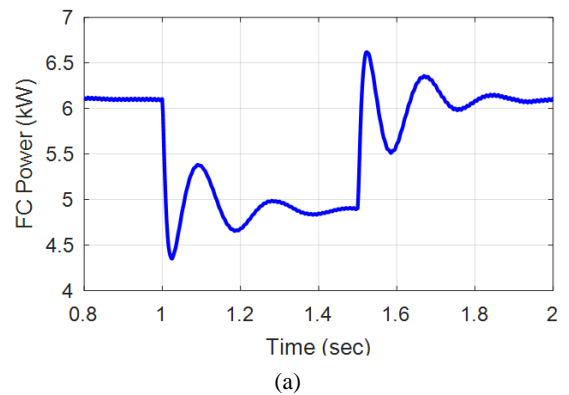

(a)

(b)

Figure 16. The generated and injected power to the grid, (a) fuel cell generated power, (b) grid injected power

and the grid and prevents significant transient fluctuations from the fuel cell side to the grid.

One of the crucial goals of grid-connected power conditioning systems is to inject high-quality current into the grid. Fig. 17(a) demonstrates the voltage at the point of common coupling (PCC) and the grid injection current of the under-study PEMFC power conditioning system. According to Fig. 17(b), the quality of the grid-injected current is outstanding, and its total harmonic distortion is 1.73%. The significant part of the negligible harmonic present in the grid-injected current is the low-order harmonic caused by the fluctuations and distortions of the fuel cell output. It can be seen from Fig. 17 that the injected current into the network is in phase with the voltage to obtain a unity power factor. Meanwhile, at t = 1 sec, the fuel flow decreased. This sudden change did not affect the performance and quality of the injected current to the network, and only the range of grid injected current was reduced by 20% from 37.5 A to 30 A.

(a)

(b)
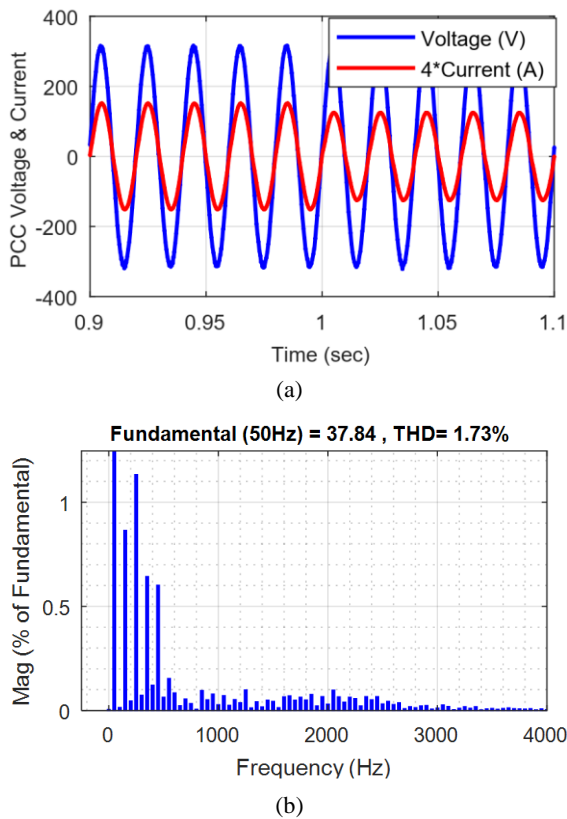
Figure 17. (a) The PCC voltage and the grid-injected current, (b) harmonic spectrum of the grid-injected current

(a)

(b)

(c)
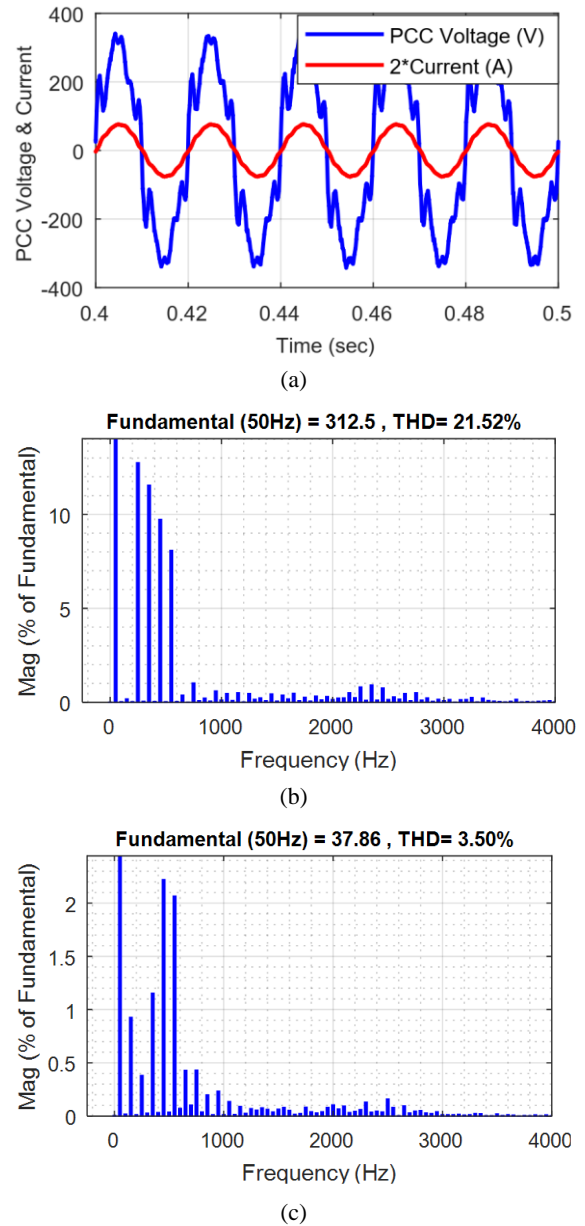
Figure 18. (a) PCC harmonics-polluted voltage and injected current to the network, (b) THD of the PCC voltage, (c) THD of the injected current to the network

One of the characteristics of weak networks, in addition to the wide range of impedance change of such networks, is the possibility of high harmonics at the PCC of the inverter. The large size of the network impedance was investigated in the previous simulations, and all the simulation results were evaluated for a pure inductive impedance equal to $L_g = 2.6 \ mH$. To check the performance of the proposed fuel cell power conditioning system in

harmonic conditions, the network voltage containing a high percentage of low-order harmonics is considered. Fig. 18 shows the high-harmonic voltage at the PCC of the inverter. In such a situation, the proposed control method can maintain the stability of the fuel cell power conditioning system and inject current with suitable quality into the network. The harmonic distortion of the grid-injected current in the harmonics-polluted network is 3.5%, a convenient value for such a network. Fig. 18(a) shows the harmonic contaminated voltage of the PCC and the injected current to the network in such conditions, Figure 18(b) displays the harmonic distortion of the PCC voltage, and Fig. 18(c) shows the harmonic distortion of the grid injected current.

Table 5 compares the proposed damping method with current methods used to improve the performance of grid-connected inverter control systems. The compared references are evaluated in terms of control method, number of sensors used, and the effect of delay. Additionally, the THD value of the current injected into the grid under the conditions assumed in this paper is also provided in Table 5. It should be noted that the purpose of presenting the THD value is solely to provide a comprehensive comparison. However, different conditions considered in each reference mean that the results in terms of THD values cannot be fairly compared directly. In general, according to relevant standards, the harmonic distortion of the current injected into the grid for low-voltage networks should not exceed 5%, which is observed in all references.

Table 5: Comparison of the proposed method with recently published articles

Reference	Control Strategy	Grid Side Sensors Count	Delay effect	THD Value
Ref [4]	Feedback Capacitor Voltage and Resonant Proportionality	2	☑	1.77%
Ref [19]	Virtual Impedance & Capacitor Current Feedback	3	☑	1.76%
Ref [34]	Active Damping	3	☑	2.1%
Ref [35]	Feedback Parallel Feedforward	3	X	2.87%
Ref [36]	Inverter Current Feedback and Active Damping	3	X	1.39%
Ref [37]	Resonant Proportionality	3	X	2.88%
Ref [38]	Capacitor Voltage Feedback	2	☑	3.47%
Ref [39]	LMI-LQR Current Control	3	☑	2.43%
Proposed	Phase Compensator on Capacitor Current Feedback Active Damping	2	☑	1.73%

6. Conclusion

The voltage source inverters are used to transfer the power of fuel cells to the low-voltage grid. LCL-type grid-connected inverters with capacitor current feedback active damping have a digital control delay problem. Since the low-voltage systems are sensitive to network impedance, the control delays may cause system instability by significant changes in network impedance. To solve this problem, a phase compensator is proposed in the capacitor current feedback path. Considering phase compensation in the capacitor current feedback increases the border frequency from $f_{sam}/6$ to almost $f_{sam}/4$, in addition, it reduces or eliminates the forbidden frequency region of LCL filter resonance as well. To ensure the correct performance of the proposed method, a step-by-step method is introduced for the design of the capacitor current feedback coefficient, parameters of the current regulator, and the phase compensator. The simulation results of the low-voltage grid-connected fuel cell power conditioning system with the proposed control method reveal that the stability of the grid-connected fuel cell system is maintained with changes in the network impedance. The quality of the injected current to the network in the ideal network is 1.37%, and in the severe harmonic network it 3.5%, which indicates the proper performance of the proposed control system. As a suggestion for future work, the extension of the single-phase system to three-phase can be mentioned where the challenges of the proposed control system in the three-phase network is investigated. Also, the

hardware implementation of the system under study is another future direction of this study.

Nomenclature

A	*Tafel* slope
AC	Alternating Current
b	Lead compensator parameter
C	Filter capacitor
C_{DC}	DC link capacitor
DC	Direct Current
f_o	Fundamental frequency
f_{sw}	Switching frequency
f_{res}	Resonance frequency
GH_{RCR-D}	Current loop gain
$f_{b,R-R}$	Border frequency of R_{CCF}
$f_{b,X-R}$	Border frequency of X_{CCF}
f_{res_LCL}	Resonance frequency of the LCL filter
f_{sam}	Sampling frequency
G_c	Transfer function of compensator
G_h	Pulse width modulation delay
G_i	Current regulator
H_{i1}	CCF current coefficient
H_{i2}	grid current coefficient
I^*	Amplitude of the grid reference current
i_o	Exchange current
L_g	grid impedance
L_1	inverter side inductor
L_2	Grid side inductor
N	number of cells
P_o	Output power
PCC	Point of common coupling
PLL	Phase locked loop
PWM	Pulse Width Modulation
R_{ad}	Equivalent virtual resistance without considering the digital control delay
RHP	Right half plane
THD	Total Harmonic Distortion
R_{CCF}	Equivalent resistance of Y_{ad-R-D}
T_{com_L}	Transfer function of the first-order derivative compensator
$T_{com,LL}$	Transfer function of the lead-lag compensator
T_{sam}	Sampling period
θ	Phase of the grid reference current
V_d	absolute polarization voltage drop
V_{fc}	Output voltage of the fuel cell stack
V_{oc}	open circuit voltage of fuel cell
V_{Ω}	resistive voltage drop of fuel cell
v_g	Network alternative voltage
v_{inv}	Inverter output voltage
VSI	Voltage Source Inverter
V_{tri}	Peak of the triangular carrier amplitude
ω_{res_LCL}	Resonance angular frequency of the LCL filter
X_{CCF}	Equivalent reactance of Y_{ad-R-D}
Y_{ad-R-D}	Equivalent virtual admittance due to CCF AD
Z_{ad-R-D}	Equivalent virtual impedance due to CCF AD
Z_g	Network impedance

REFERENCES

[1] Hosseinpour, M., Dastgiri, A., & Shahparasti, M. (2024). Design and Analysis of a Power Quality Improvement System for Photovoltaic Generation Based on LCL-Type Grid Connected Inverter. *International Journal of Engineering*, *37*(2), 252-267. https://doi.org/10.5829/ije.2024.37.02b.04

[2] Hosseinpour, M., Akbari, R., & Shahparasti, M. (2024). A Robust Photovoltaic Power Conditioning System Connected to Weak Grid Through Virtual Impedance Shaping. *Journal of Solar Energy Research*, 9(2), 1870-1886. https://doi.org/10.22059/jser.2024.369348.1364

[3] Mirzakhani, A., & Pishkar, I. (2023). Finding the best configuration of an off-grid PV-Wind-Fuel cell system with battery and generator backup: a remote house in Iran. *Journal of Solar Energy Research*, 8(2), 1380-1392. https://doi.org/10.22059/jser.2023.349781.1259

[4] Hosseinpour, M., Sabetfar, T., & Shahparasti, M. (2024). Grid- tied PEMFC power conditioning system based on capacitor voltage thorough feedback procedure in a weak and

harmonics- polluted network. *Energy Science & Engineering*, *12*(1), 149-167. https://doi.org/10.1002/ese3.1624

[5] Kumar, L., Manoo, M. U., Ahmed, J., Arıcı, M., & Awad, M. M. (2025). Comparative techno-economic investigation of hybrid energy systems for sustainable energy solution. *International Journal of Hydrogen Energy*, 104, 513-526. https://doi.org/10.1016/j.ijhydene.2024.05.369

[6] Han, B., Bai, C., Lee, J. S., & Kim, M. (2018). Repetitive controller of capacitor-less current-fed dual-half-bridge converter for grid-connected fuel cell system. *IEEE Transactions On Industrial Electronics*, *65*(10), 7841-7855. https://doi.org/10.1109/TIE.2018.2804898

[7] A Sabir, A. (2019). A PLL-free robust control scheme with application to grid-connected fuel cell DGs under balanced and unbalanced conditions. *Sustainable Energy Technologies and Assessments*, *31*, 64-76. https://doi.org/10.1016/j.seta.2018.12.001

[8] Baltacı, K., Ertekin, D., & Bayrak, G. (2024). Design and experimental validation of an artificial neural network-SVPWM controller for a novel micro grid-tied fuel cell-based 3-phase boost inverter. *International Journal of Hydrogen Energy*, *52*, 1247-1265. https://doi.org/10.1016/j.ijhydene.2023.10.291

[9] Rasekh, N., & Hosseinpour, M. (2020). LCL filter design and robust converter side current feedback control for grid-connected Proton Exchange Membrane Fuel Cell system. *International Journal of Hydrogen Energy*, *45*(23), 13055-13067. https://doi.org/10.1016/j.ijhydene.2020.02.227

[10] A Mahmoudian, A., Garmabdari, R., Bai, F., Guerrero, J. M., Mousavizade, M., & Lu, J. (2024). Adaptive power-sharing strategy in hybrid AC/DC microgrid for enhancing voltage and frequency regulation. *International Journal of Electrical Power & Energy Systems*, *156*, 109696. https://doi.org/10.1016/j.ijepes.2023.109696

[11] Aalizadeh, F., Hosseinpour, M., Dejamkhooy, A., & Shayeghi, H. (2021). Two-stage control for small-signal modeling and power conditioning of grid- connected quasi-Z-Source inverter with LCL filter for photovoltaic generation. *Journal of Operation and Automation in Power Engineering*, *9*(3), 242-255. https://doi.org/10.22098/joape.2021.7674.1546

[12] Hosseinpour, M., Sabetfar, T., Dejamkhooy, A., & Shahparasti, M. (2023). Design and control of LCL-type grid-tied PV power conditioning system based on inverter and grid side currents double feedback. *International Journal of Modelling and Simulation*, 1-21. https://doi.org/10.1080/02286203.2023.2204319

[13] Rasekh, N., Hosseinpour, M., Dejamkhooy, A., & Akbarimajd, A. (2021). Robust power conditioning system based on LCL-type quasi-Y-source inverter for grid connection of photovoltaic arrays. *International Journal of Automation and Control*, *15*(6), 692-709. https://doi.org/10.1504/IJAAC.2021.118526

[14] Rasekh, N., & Hosseinpour, M. (2020). Adequate tuning of LCL filter for robust performance of converter side current feedback control of grid connected modified–Y-source inverter. *International Journal of Industrial Electronics Control and Optimization*, *3*(3), 365-378. https://doi.org/10.22111/ieco.2020.32122.1221

[15] Hosseinpour, M., Asad, M., & Rasekh, N. (2021). A step-by-step design procedure of a robust control design for grid-connected inverter by LCL filter in a weak and harmonically distorted grid. *Iranian Journal of Science and Technology, Transactions of Electrical Engineering*, *45*, 843-859. https://doi.org/10.1007/s40998-021-00414-z

[16] Wang, X., Blaabjerg, F., & Loh, P. C. (2016). Grid-current-feedback active damping for LCL resonance in grid-connected voltage-source converters. *IEEE Transactions on Power Electronics*, *31*(1), 213-223. https://doi.org/10.1109/TPEL.2015.2411851

[17] Hosseinpour, M., Seifi, E., Khorramdel, H., & Sajedi, S. (2025). Design and Analysis of a Photovoltaic Power Conditioning System Using Grid Voltage Feedforward Procedure in Weak Grid Condition. *International Journal of Engineering*. 38(2), 394-320. https://doi.org/10.5829/ije.2025.38.02b.05

[18] Rasekh, N., Rahimian, M. M., Hosseinpour, M., Dejamkhooy, A., & Akbarimajd, A. (2019, February). A step by step design procedure of PR controller and capacitor current feedback active damping for a LCL-type grid-tied T-type inverter. In *2019 10th International Power Electronics, Drive Systems and Technologies Conference (PEDSTC)* (pp. 612-617). https://doi.org/10.1109/PEDSTC.2019.8697853

[19] Hosseinpour, M., & Kholousi, A. (2023). Design and Analysis of LCL-type Grid-

Connected PV Power Conditioning System Based on Positive Virtual Impedance Capacitor-Current Feedback Active Damping. *Journal of Solar Energy Research*, 8(2), 1497-1515. https://doi.org/10.22059/jser.2023.357089.1286

[20] Hosseinpour, M., & Rasekh, N. (2019). A single-phase grid-tied PV based trans-z-source inverter utilizing LCL filter and grid side current active damping. *Journal of Energy Management and Technology*, 3(3), 67-77. http://dx.doi.org/10.22109/jemt.2019.169380.1150

[21] Upadhyay, N., Padhy, N. P., & Agarwal, P. (2024). Grid-Current Control with Inverter-Current Feedback Active Damping for LCL Grid-Connected Inverter. *IEEE Transactions on Industry Applications*. 60(1), 1738 – 1749. https://doi.org/10.1109/TIA.2023.3316997

[22] Wang, B., Xu, Y., Shen, Z., Zou, J., Li, C., & Liu, H. (2017). Current control of grid-connected inverter with LCL filter based on extended-state observer estimations using single sensor and achieving improved robust observation dynamics. *IEEE Transactions on Industrial Electronics*, 64(7), 5428-5439. https://doi.org/10.1109/TIE.2017.2674600

[23] López-Alcolea, F. J., Molina-Martínez, E. J., Torres, A. P., Vázquez, J., & Roncero-Sánchez, P. (2023). 2DOF-based current controller for single-phase grid-connected voltage source inverter applications. *Applied Energy*, 342, 121179. https://doi.org/10.1016/j.apenergy.2023.121179

[24] Campos, B. F. D. A., Rolim, L. G. B., Encarnação, L. F., & Tricarico, T. C. (2023, November). Delay Compensation on Optimal Switching Vector Model Predictive Control Applied to a Grid-Forming Inverter with an Output LC Filter in an Islanded Microgrid. In *2023 15th IEEE International Conference on Industry Applications (INDUSCON)* (pp. 1410-1417). https://doi.org/10.1109/INDUSCON58041.2023.10374659

[25] Huang, M., Wang, X., Loh, P. C., & Blaabjerg, F. (2016). LLCL-filtered grid converter with improved stability and robustness. *IEEE Transactions on Power Electronics*, 31(5), 3958-3967. https://doi.org/10.1109/TPEL.2015.2467185

[26] Pan, D., Ruan, X., Bao, C., Li, W., & Wang, X. (2014). Capacitor-current-feedback active damping with reduced computation delay for improving robustness of LCL-type grid-

connected inverter. *IEEE Transactions on Power Electronics*, 29(7), 3414-3427. https://doi.org/10.1109/TPEL.2013.2279206

[27] Hosseinpour, M., Kholousi, A., & Poulad, A. (2022). A robust controller design procedure for LCL- type grid- tied proton exchange membrane fuel cell system in harmonics- polluted network. *Energy Science & Engineering*, 10(10), 3798-3818. https://doi.org/10.1002/ese3.1250

[28] He, Y., Wang, X., Ruan, X., Pan, D., Xu, X., & Liu, F. (2019). Capacitor-current proportional-integral positive feedback active damping for LCL-type grid-connected inverter to achieve high robustness against grid impedance variation. *IEEE Transactions on Power Electronics*, 34(12), 12423-12436. https://doi.org/10.1109/TPEL.2019.2906217

[29] Chen, C., Xiong, J., Wan, Z., Lei, J., & Zhang, K. (2017). A time delay compensation method based on area equivalence for active damping of an LCL-type converter. *IEEE Transactions on Power Electronics*, 32(1), 762-772. https://doi.org/10.1109/TPEL.2016.2531183

[30] İnci, M. (2020). Active/reactive energy control scheme for grid-connected fuel cell system with local inductive loads. *Energy*, 197, 117191.

[31] Wang, X., Bao, C., Ruan, X., Li, W., & Pan, D. (2014). Design considerations of digitally controlled LCL-filtered inverter with capacitor-current-feedback active damping. *IEEE Journal of Emerging and Selected Topics in Power Electronics*, 2(4), 972-984. https://doi.org/10.1109/JESTPE.2014.2350262

[32] Li, Y., Gao, J., Zhang, Z., & Wang, Q. (2024). Model-Based and Model-Free Predictive Active Damping for LCL-Type Active-Front-End Rectifiers. *IEEE Transactions on Industrial Electronics*, 7(10), 11754-11765. https://doi.org/10.1109/TIE.2023.3344848

[33] Zhang, L., Ruan, X., & Ren, X. (2015). Second-harmonic current reduction and dynamic performance improvement in the two-stage inverters: An output impedance perspective. *IEEE Transactions on Industrial Electronics*, 62(1), 394-404. https://doi.org/10.1109/TIE.2014.2331015

[34] Chen, R., Zeng, J., Huang, X., & Liu, J. (2023). An H∞ filter based active damping control strategy for grid-connected inverters with LCL filter applied to wind power system. *International Journal of Electrical Power & Energy Systems*, 144, 108590. https://doi.org/10.1016/j.ijepes.2022.108590

[35] Khan, D., Zhu, K., Hu, P., Waseem, M., Ahmed, E. M., & Lin, Z. (2023). Active damping of LCL-Filtered Grid-Connected inverter based on parallel feedforward compensation strategy. *Ain Shams Engineering Journal*, 14(3), 101902. https://doi.org/10.1016/j.asej.2022.101902

[36] Qian, W., Yin, J., & Chen, Z. (2024). Stability Comparison of Grid-Connected Inverters Considering Voltage Feedforward Control in Different Domains. *Applied Sciences*, 14(19), 9026. https://doi.org/10.3390/app14199026

[37] Yang, Y., Guo, X., Lu, Z., Hua, C., Castilla, M., & Blaabjerg, F. (2020). Advanced control of grid-connected inverters for proton exchange membrane fuel cell system. *International Journal of Hydrogen Energy*, 45(58), 33198-33207.
https://doi.org/10.1016/j.ijhydene.2020.09.130

[38] Faiz, M. T., Khan, M. M., Jianming, X., Ali, M., Habib, S., Hashmi, K., & Tang, H. (2019). Capacitor voltage damping based on parallel feedforward compensation method for LCL-filter grid-connected inverter. *IEEE Transactions on Industry Applications*, 56(1), 837-849.
https://doi.org/10.1109/TIA.2019.2951115.

[39] Bimarta, R., & Kim, K. H. (2020). A robust frequency-adaptive current control of a grid-connected inverter based on LMI-LQR under polytopic uncertainties. *IEEE Access*, 8, 28756-28773.
https://doi.org/10.1109/ACCESS.2020.2972028.